Improved Wear and Corrosion Resistance of Microarc Oxidation Coatings on Ti–6Al–4V Alloy with Ultrasonic Assistance for Potential Biomedical Applications

Cheng Xu, Liang-Yu Chen,* Chuan-Bo Zheng,* Hong-Yue Zhang, Cui-Hua Zhao, Ze-Xin Wang, Sheng Lu, Jin-Wei Zhang, and Lai-Chang Zhang*

Although microarc oxidation is frequently used in producing wear- and corrosion-resistant coatings on Ti and Ti alloys for biomedical applications, the formation of nonuniform microstructure of the coatings is still unavoidable. To overcome this drawback, this work adopts ultrasonic assistance in the microarc oxidation of Ti–6Al–4V and systematically investigates the influences of ultrasonic treatment with different durations on the coating microstructures and resultant properties. The positive effects of ultrasonic, such as cavitation effect, sound flow effect, and mechanical effect, accelerate the cooling rate of electrolyte and promote the homogeneity of the solute on the sample surface. Therefore, the ultrasonic-assisted coatings exhibit uniform microstructures with fewer cracks and therefore improve performances. For instance, compared with the counterpart without ultrasonic assistance, the ultrasonic-assisted coating with 15 min duration demonstrates 25.1% lower mass loss in the tribology test and half corrosion density in Hank's solution. Such results indicate that ultrasonic assistance in microarc oxidation of Ti–6Al–4V can homogenize the microstructures of coatings and enhance their corrosion resistance and wear resistance in human body.

1. Introduction

Because of their outstanding properties, such as good biocompatibility, high specific strength, and superior corrosion resistance, titanium (Ti) and its alloys have received considerable attention during recent years.[1–8] Among various Ti alloys, Ti–6Al–4V alloy, which belongs to α + β dual-phase Ti alloys, possesses good fatigue resistance, strength, and corrosion resistance.[9–13] Therefore, Ti–6Al–4V alloys are applied in biological fields, especially for hard tissue replacements (such as orthopedic implants).[14–16] However, the disadvantages of Ti–6Al–4V alloys, including low hardness, strong biological inertness, and poor wear resistance, are also apparent, which restrict their further applications. Therefore, surface modifications are often recommended to improve biological activity, hardness, and wear resistance of Ti–6Al–4V alloys.[17–21]

Generally, surface modifications of Ti and its alloys involve extensive techniques.[22–24] Among the surface modifications, microarc oxidation is a commonly effective surface modification method.[25–28] Microarc oxidation, which is also called plasma electrolytic oxidation (PEO) or microplasma oxidation (MPO), produces oxide coatings on the surface of metals in various electrolytes using a high voltage of about 150–1000 V.[29,30] When high voltage is applied, high temperature and high pressure are instantaneously generated on the metal surface.[31] As a result, the reactions between the metal substrate and electrolyte take place and an oxide coating is therefore produced. Meanwhile, the formed oxide coating has a porous structure which is very suitable for cell adhesion.[32,33] In recent years, constant voltage mode, constant current mode, and two-step voltage-increasing mode have formed the mainstream modes of microarc oxidation.[34–37] The constant voltage means that a constant voltage value is used to conduct during microarc oxidation, while the power for coating growth is insufficient in the late stage. Therefore, the thickness of the produced

C. Xu, Prof. L.-Y. Chen, Prof. C.-B. Zheng, Prof. H.-Y. Zhang, Z.-X. Wang, Prof. S. Lu, J.-W. Zhang
School of Materials Science and Engineering
Jiangsu University of Science and Technology
Mengxi Road 2#, Zhenjiang 212003, China
E-mail: lychen@just.edu.cn; cbzheng@just.edu.cn

Prof. C.-B. Zheng
School of Metallurgical and Materials Engineering
Zhangjiagang Campus of Jiangsu University of Science and Technology
Zhangjiagang 215600, China

⃝iD The ORCID identification number(s) for the author(s) of this article can be found under https://doi.org/10.1002/adem.202001433.

Dr. C.-H. Zhao
Guangxi Key Laboratory of Processing for Non-ferrous Metals and Featured Materials
Guangxi University
Nanning 530004, China

Prof. L.-C. Zhang
School of Engineering
Edith Cowan University
270 Joondalup Drive, Joondalup, Perth, WA 6027, Australia
E-mail: l.zhang@ecu.edu.au, lczhangimr@gmail.com

ADVANCED
SCIENCE NEWS
www.advancedsciencenews.com

ADVANCED
ENGINEERING
MATERIALS
www.aem-journal.com

coating is too thin at this mode. The two-step voltage-increasing mode uses two different voltages during microarc oxidation. When the first applied voltage cannot break down oxide layer, an increased voltage is subsequently used to maintain the reaction. The two-step voltage-increasing mode would consume high energy and generate a high current in the late stage, leading to the release of excessive heat. The constant current refers to the fact that a constant current density is applied during microarc oxidation process. The coating formed by the constant current mode is thicker than that formed by the constant voltage and denser than that formed by the two-step voltage-increasing mode. Li et al.[25] pointed out that the microarc oxidation layer on pure Ti is prone to adsorb Ca^{2+} and P^{5+} ions compared with pure Ti. Previous study demonstrates that microarc oxidation has positive influences on the properties of Ti and Ti alloys, especially for biomedical applications.

Although the microarc oxidation process is capable of forming an oxide coating with better corrosion resistance and wear resistance, the produced coating also presents some drawbacks, such as uneven microstructure and thickness.[17] To overcome these drawbacks, many researchers found that the assistance of ultrasonic in the microarc oxidation process can improve the quality of produced oxide coatings, owing to the positive effects of ultrasonic, including cavitation effect, sound flow effect, thermal effect, and mechanical effect.[38–40] When ultrasonic is used in microarc oxidation process, the cavitation effect plays an important role in the formation of oxide coating. The cavitation effect refers to a dynamic process of the production, growth, and collapse of cavitation bubbles in the liquid. Such bubbles vibrate under the action of sound waves and would break down when the sound pressure reaches a certain value. This phenomenon greatly increases the reaction rate of heterogeneous phases, accelerates the diffusion of reactants and products, and promotes the formation of new solid phases.[34,40,41] For aluminum and magnesium alloys, researchers have found that the ultrasonic-assisted samples have a higher thickness, fewer microcracks, and more homogeneous microporous structures. For example, for 6061 Al alloy, the maximum thickness of coating with ultrasonic assistance is 7 μm (15%) thicker than the counterpart without ultrasonic assistance. The largest pore size of coating with ultrasonic assistance is about 5 μm, which is significantly smaller than that (12.1 μm) of the counterpart without ultrasonic assistance.[41] For Mg alloy, the corrosion potential of the sample with ultrasonic assistance is −0.353 V, which is significantly higher than that of the counterpart without ultrasonic assistance (−1.098 V).[34] As such, such coatings have higher microhardness, better wear resistance, and better corrosion resistance.[34,41,42] However, rare literature has investigated the microarc oxidation of Ti–6Al–4V alloy with ultrasonic assistance for potential biomedical applications.[43] The effects of ultrasonic assistance on the detailed microstructural features of the produced oxide coatings on Ti–6Al–4V alloy are still not understood. Furthermore, considering the better performances of microarc oxidation coatings on Al alloys and Mg alloys produced with ultrasonic assistance and broad applications of Ti alloys in biomedical applications, it is highly significant to further investigate the performance of microarc oxidation coatings on Ti–6Al–4V using ultrasonic assistance. This would also shed insight into the effect of ultrasonic assistance on the microarc oxidation of

Ti–6Al–4V and give a proposal to further improve the properties of microarc oxidation coatings on Ti–6Al–4V for potential biomedical applications.

As such, this work used ultrasonic assistance in the microarc oxidation process of Ti–6Al–4V alloy. The microarc oxidation process of Ti–6Al–4V without ultrasonic assistance was used as the reference for comparison. The microstructures, corrosion, and wear properties of all produced coatings were investigated. Moreover, the mechanism of ultrasonic assistance in the microarc oxidation process was also discussed. In addition, the cell count experiment was conducted to evaluate the biological performance of the coating samples with 15 min microarc oxidation duration.

2. Results and Discussion

2.1. Formation of Microarc Oxidation Coatings

Figure 1 shows the relationship between treatment time and voltage during the microarc oxidation process. The subgraphs in Figure 1a-c are the magnified images that show the voltage differences between MAO and UMAO samples with microarc oxidation duration from 40 to 200 s. The observed change in the voltage is in line with the definition of microarc oxidation,[44] where the total microarc oxidation process can be divided into three stages, as shown in Figure 1. In the stage I, the voltage linearly increases with time at the largest slope, which is consistent with the traditional anodizing process. In the stage II, the surface of the sample is broken down, and the voltage gradually increases at a lower rate as compared with that in the first stage. In the stage III, microdischarge occurs over the entire sample surface, and the voltage increases at a very low rate over time.[20] For all samples, the voltage sharply increases at a slope of 4.0–4.4 V s^{-1} up to the breakdown voltage in stage I (0 to about 50 s). In this stage, sparks are not presented, but a large number of oxygen bubbles are observed on the sample surfaces, which is consistent with traditional anodization.[45] Ultrasonic can produce bubbles in the electrolyte. The cavitation effect of ultrasonic leads to the growth of those bubbles, while the ultrasonic-produced oscillation makes the bubbles shrink. Finally, those bubbles would break. Therefore, the bubbles on the samples grow and break. Such a phenomenon produces a high-temperature/high-pressure microenvironment on the sample surfaces, providing additional energy and reducing the breakdown voltage.[42] The breakdown voltage is defined as the lowest voltage which can break down the oxide coating formed on the substrate.[35] As shown in Figure 1, the breakdown voltage (the beginning of nonlinear segment) of ultrasonic-assisted samples is around 213 V and the untreated sample is around 230 V. Afterward, the voltage exceeds the breakdown voltage, which means the commence of stage II (50–200 s). As described in the insets in Figure 1a-c, the ultrasonic-assisted samples have lower voltages than the untreated samples during 40–200 s. When the reaction enters stage II, small and dense sparks begin to form on the sample surfaces, illustrating the commence of microarc oxidation. In this stage, the amount of oxygen bubbles significantly increases with the increase in the duration. When the microarc oxidation process reaches about 200 s, the voltages
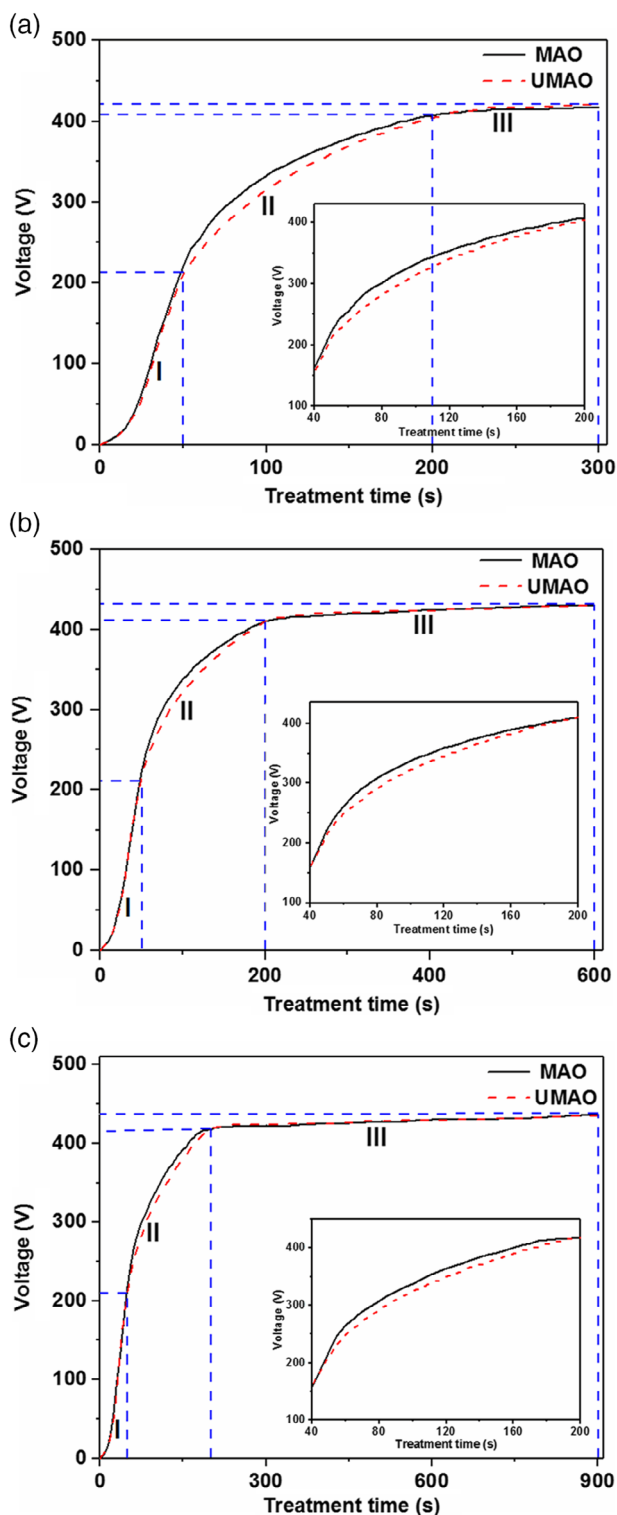
Figure 1. Change in voltage versus treatment time for all microarc oxidation samples with or without ultrasonic assistance after different durations: a) 5 min, b) 10 min, and c) 15 min. MAO indicates the microarc oxidized samples without ultrasonic assistance; UMAO means the microarc oxidized samples with ultrasonic assistance.

of all samples are gradually stabilized. In the meantime, large and white sparks gradually replace tiny sparks on the sample surfaces. This phenomenon indicates that the reaction enters stage III (200 s to the end of the experiment).[45] Late in this stage, the number of large sparks decreases gradually and some small sparks remain on the sample surfaces.[44,45]

2.2. Microstructural Characterizations

The cross-sectional morphologies of samples after different durations are shown in **Figure 2** and their corresponding thicknesses are shown in **Figure 3**. As shown in Figure 2a,c,e, there are many cracks and pores in MAO samples. High voltage generated in the process can provide significant energy on the surface of the sample and produce a large amount of heat to melt the metal substrate. Before complete solidification of molten metal, the subsequent ceramic layer has already formed.[43] However, part of molten metal cannot curdle in time. Consequently, the solidification of molten metal may lead to the shrinkage of the ceramic layer. Meanwhile, as no metal fills the voids produced by shrinkage, such voids may develop cracks and pores. When the molten metal solidifies, many regions of the coating shrink simultaneously, and the shrinkage takes place among these regions. Finally, cracks are produced.[43] Figure 2b,d,f shows the different cross-sectional morphologies of UMAO samples. Undergoing the same duration, the UMAO sample has a higher thickness and exhibits a more compact cross section compared with the MAO counterpart. The reason for the higher thickness is shown in Figure 3. Both the number and size of pores and cracks decrease; the pores become smaller as the duration increases. Therefore, one can conclude that the UMAO samples have smaller and fewer cracks and pores than the MAO counterparts. In addition, the differences in the thickness of MAO samples become more evident with increasing the duration, indicating the increase in their surface undulation (Figure 2a,c,e). By contrast, the surfaces of the UMAO counterparts are relatively smooth when subjected to the same duration (Figure 2b,d,f). Such results are also shown in Figure 3. The standard deviations of thickness are 0.4 and 0.3 µm for MAO-5 and UMAO-5, 0.8 and 0.6 µm for MAO-10 and UMAO-10, and 1.8 and 0.8 µm for MAO-15 and UMAO-15, respectively. Therefore, the UMAO samples have more uniform thickness than the MAO samples. It is known that ultrasonic can stir the electrolyte and accelerate the flow of liquid, resulting in fast cooling of electrolyte during the MAO process. Therefore, the molten metal can be solidified before the formation of subsequent ceramic layer. As a result, ultrasonic assistance can reduce the production of internal flaws in the UMAO coatings.

As shown in Figure 3, the thicknesses of MAO and UMAO coatings increase as extending the duration. Furthermore, by comparing the thicknesses of MAO-5 (10.9 ± 0.4 µm) and MAO-10 (15.2 ± 0.8 µm), the increment in thickness is about 4.3 µm. However, the increment in thickness is only about 2.9 µm between MAO-15 (18.1 ± 1.8 µm) and MAO-10. This phenomenon has been reported in the literature; the growth rate of MAO coating would decline as the duration increases.[43] Similar
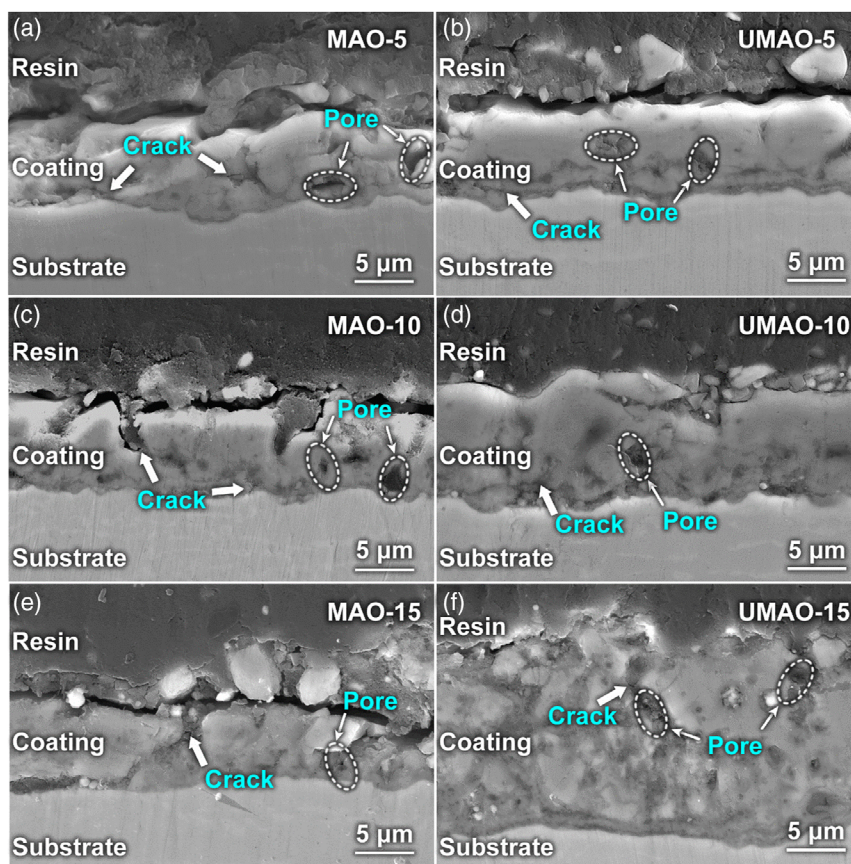
Figure 2. Scanning electron microscope (SEM) images of cross-sectional samples after different durations: a) MAO-5, b) UMAO-5, c) MAO-10, d) UMAO-10, e) MAO-15, and f) UMAO-15. MAO-5, MAO-10, and MAO-15 indicate the microarc oxidized samples without ultrasonic assistance under the duration of 5, 10, and 15 min; UMAO-5, UMAO-10, and UMAO-15 mean the microarc oxidized samples with ultrasonic assistance under the duration of 5, 10, and 15 min.
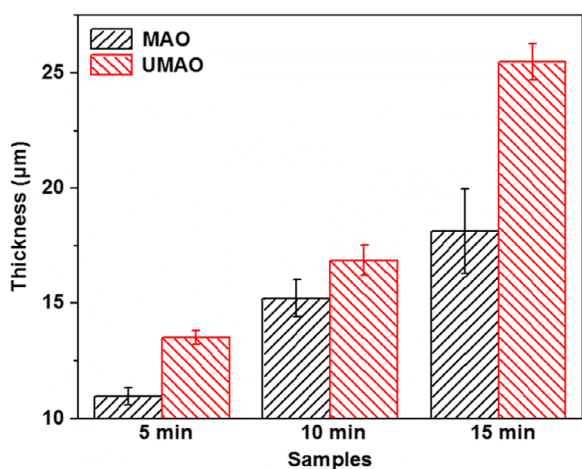

Figure 3. Thicknesses of MAO and UMAO samples after different durations. MAO indicates the microarc oxidized samples without ultrasonic assistance; UMAO means the microarc oxidized samples with ultrasonic assistance.

to the MAO samples, a relatively large change in the thickness of UMAO samples is observed from 5 min ($13.5 \pm 0.3\,\mu m$) to 10 min ($16.8 \pm 0.6\,\mu m$). However, when the duration prolongs

to 15 min, the thickness of the UMAO sample surges to $25.4 \pm 0.8\,\mu m$. Because the UMAO-15 is too thick, the sparks cannot break down the coating. For the abnormal increase in the thickness of UMAO-15, the voltage may not play a critical role in the mid-to-late stage of the microarc oxidation process. It is speculated that the ultrasonic assistance may lead to sedimentation on the coating surface due to the combination of sound flow effect and thermal effect. Therefore, the UMAO coating continues growing.

Based on these results shown in Figure 2 and 3, some facts can be obtained. At stage I (Figure 1), the voltage increases rapidly, which indicates the formation of a thin layer (anodization).[43] At stage II, as the sparks maintain on the surface of the sample, more molten oxides are formed via molten metal. As the microarc oxidation reaction proceeds, the oxide coating becomes thicker, which, in turn, suppresses the generation of sparks. Therefore, the discharge region decreases and the voltage increases slowly in stage II, as shown in Figure 1. Meanwhile, the growth rate of oxide coating also becomes slower than that in stage II.[43,45] Moreover, Figure 3 shows that the UMAO samples show larger average thickness than the MAO counterparts. When ultrasonic assistance was applied in the microarc oxidation process, the ultrasonic can facilitate the production of O^{2-} in the electrolyte.[34] Therefore, more O^{2-} reacts with the substrate,

ADVANCED
SCIENCE NEWS
www.advancedsciencenews.com

*ADVANCED
ENGINEERING
MATERIALS*
www.aem-journal.com

resulting in the formation of more oxides. In other words, the acoustic flow effect and mechanical effect aroused by ultrasonic can stir the electrolyte, resulting in more uniform distribution of solute. Therefore, ultrasonic assistance can effectively promote the transportation of substances on the surface of the sample. A similar phenomenon is also found in the corrosion of metallic materials in flowing solution; the flowing solution promotes the mass transfer during the corrosion process.[46] As such, the concentrations of substances, which are required to generate the oxide coating, increase after the same duration for UMAO samples. In addition, the cavitation effect of ultrasonic increases the discharge channels and enhances the formation of the melt at stage II.[42] Therefore, ultrasonic assistance would promote the growth of microarc oxidation coatings.

Figure 4 shows the surface morphologies of MAO and UMAO samples. As mentioned earlier, pores and cracks are observed for all samples. With increasing the time of microarc oxidation, higher voltage supplies more energy to make more molten oxide spurt from the arc channels. Meanwhile, the reaction is accelerated due to more energy provided, therefore more heat is generated. When the duration increases from 5 to 10 min, more energy is provided to melt more metals in MAO-10 and such molten metals fill the cracks. Consequently, the cracks in the MAO-10 are fewer and smaller than those of MAO-5 (Figure 4a,c,e). A similar scenario is found in the UMAO samples (Figure 4b,d,f). After the same duration, UMAO samples show fewer and smaller cracks compared with the MAO counterparts (Figure 4). Those features may have positive effects on the
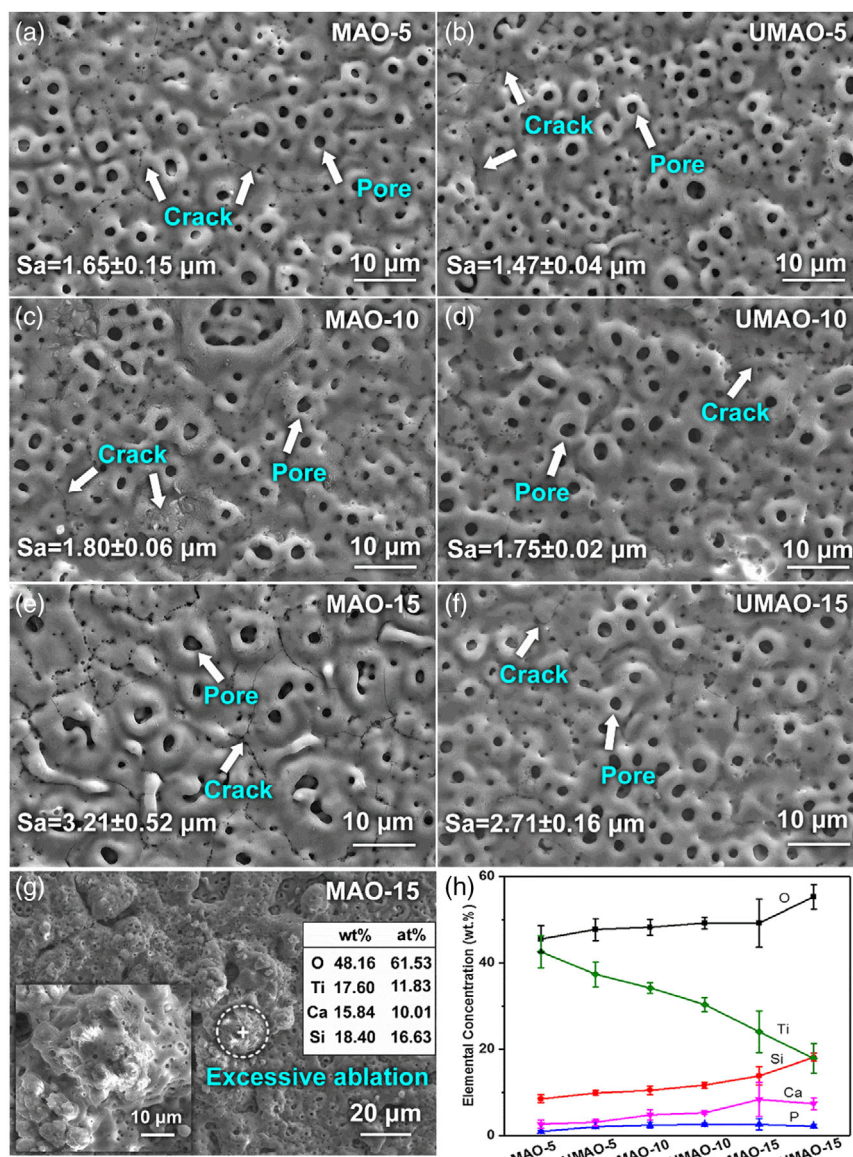

Figure 4. SEM images of sample surfaces after different durations: a) MAO-5, b) UMAO-5, c) MAO-10, d) UMAO-10, e) MAO-15, f) UMAO-15, and g) MAO-15. h) The surface elemental concentration after different durations. MAO-5, MAO-10, and MAO-15 indicate the microarc oxidized samples without ultrasonic assistance under the duration of 5, 10, and 15 min; UMAO-5, UMAO-10, and UMAO-15 mean the microarc oxidized samples with ultrasonic assistance under the duration of 5, 10, and 15 min.

ADVANCED
SCIENCE NEWS
www.advancedsciencenews.com

ADVANCED
ENGINEERING
MATERIALS
www.aem-journal.com

properties of coatings. One reason accounting for fewer and smaller cracks on the UMAO samples is the stirring effect of ultrasonic, which increases the flow rate of electrolyte. Therefore, ultrasonic leads to the homogeneous distribution of heat on the sample surface, thereby reducing the production of cracks.

Moreover, the concentrations of reactants are heterogeneous on the surfaces of samples during the microarc oxidation process. Strong reactions would take place in some regions with high concentrations of reactants. Therefore, more heat is generated in such regions. Because the ceramic coating has a poor capability of heat dissipation, the surface may ablate.[43] At low magnification, one can find many excessive ablation regions on the surface of MAO-15 (Figure 4g). The energy disperse spectroscopy (EDS) result shows that the surface of MAO-15 shows a variety of oxides of Si, Ca, P, and Ti. Such a phenomenon produces the heterogeneous distribution of elements on the sample surface. However, excessive ablation is not found in UMAO-15. The cavitation effect caused by ultrasonic could accelerate the formation of the bubbles. Such bubbles take away the heat on the surface, thereby cooling the molten oxides.[43] Furthermore, the stirring effect can promote the circulation of the electrolyte, which also accelerates the cooling of molten oxides. Therefore, the excessive ablation of coatings is absent on the surface of UMAO-15 (Figure 4f). Figure 4h shows the elemental concentrations of the sample surfaces (obtained from mapping results, now shown herein). When the duration increases, the microarc oxidation reaction continues, and the O^{2-} in the solution continuously reacts with the substrate. However, the substrate is difficult to participate in the microarc oxidation reaction when the coating thickness exceeds a certain extent. Therefore, the concentrations of Ca, P, and Si on the coating surfaces increase, and correspondingly the concentration of Ti decreases. The ultrasonic assistance can produce more O^{2-} in the solution, thereby promoting the formation of the oxides on the sample surface.[34] As such, the UMAO sample surface always has higher O concentration than the MAO counterpart surface.

Furthermore, the roughnesses (Sa) of the sample surfaces are also shown in Figure 4. When the duration increases, the roughness increases for all samples. The UMAO sample shows lower roughness than the MAO counterparts. For instance, the UMAO-15 sample has a roughness of $2.71 \pm 0.14\,\mu m$, while the MAO-15 counterpart has a roughness of $3.21 \pm 0.52\,\mu m$. As the microarc oxidation progresses, the microarc discharge becomes more severe on the sample surface due to the increased voltage until the end of stage II (Figure 1). The higher energy input increases the pore size and therefore the roughness.[25] However, the ultrasonic assistance can decrease the breakdown voltage as well as the voltage in stage II. Therefore, lower energy input during the microarc oxidation process results in lower pore size and roughness.

Figure 5 shows the porosities and the mean areas of pores for different coatings on samples. The data for MAO-15 were obtained by calculating the pores in the relatively flat regions on the MAO-15 surface (i.e., Figure 4e). As shown in Figure 5, the sizes of pores of both MAO and UMAO samples increase and their porosities also slightly increase with the extension of duration. The pores are remnants of arc channels after the microarc oxidation process. With the augment of the duration,
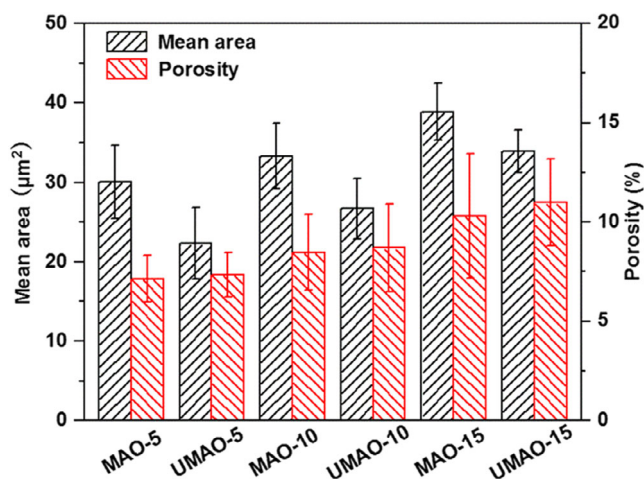

Figure 5. Porosities and mean areas of pores for different samples. MAO-5, MAO-10, and MAO-15 indicate the microarc oxidized samples without ultrasonic assistance under the duration of 5, 10, and 15 min; UMAO-5, UMAO-10, and UMAO-15 mean the microarc oxidized samples with ultrasonic assistance under the duration of 5, 10, and 15 min.

the voltage increases (Figure 1), thereby producing more and larger arc channels on the sample surface and increasing the number and the sizes of pores (Figure 5).

2.3. Phase Constituents of the Coatings

Figure 6 shows the X-ray diffraction (XRD) patterns of all samples. TiO_2 (rutile and anatase phases) are the main phase constituents of both MAO and UMAO coatings. The coating is mainly composed of TiO_2, and the contents of Ca and P in the coating are significantly low. Therefore, the compounds of Ca and P are absent in the XRD patterns. With increasing the duration, the intensity of the substrate decreases, indicating the growth of
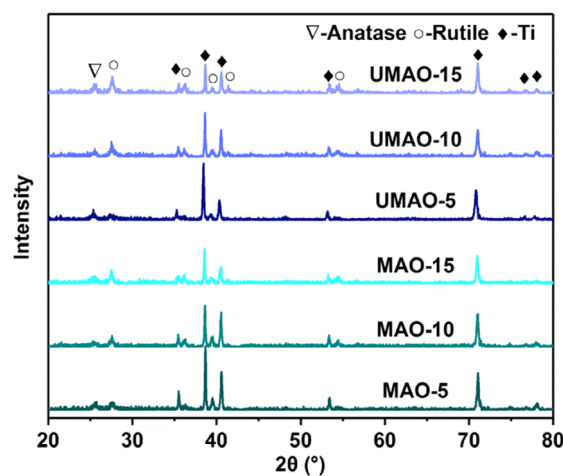

Figure 6. XRD patterns of MAO and UMAO coatings. MAO-5, MAO-10, and MAO-15 indicate the microarc oxidized samples without ultrasonic assistance under the duration of 5, 10, and 15 min; UMAO-5, UMAO-10, and UMAO-15 mean the microarc oxidized samples with ultrasonic assistance under the duration of 5, 10, and 15 min.

Table 1. Volume fractions of anatase and rutile phases and their crystallite sizes in the MAO and UMAO samples. The data were calculated by the XRD patterns in Figure 6.

Samples	Time [min]	Volume fraction [%]			Crystallite size [nm]	
		Anatase	Rutile	Ti	Anatase (101)	Rutile (110)
MAO	5	6.18	16.80	77.02	12.16	6.03
	10	7.03	23.04	69.93	15.40	9.05
	15	7.81	30.14	62.05	15.93	11.65
UMAO	5	7.94	23.19	68.87	4.64	3.90
	10	8.13	29.40	62.47	5.82	5.04
	15	8.46	33.86	57.68	7.07	5.95

coatings. **Table 1** shows the volume fractions of rutile and anatase phases in the coatings. Although the volume fraction of rutile gradually increases with the growth of coating, no apparent difference is found for both UMAO and MAO counterparts. Therefore, one can conclude that the ultrasonic has almost no effect on the phase constituents of coatings. Meanwhile, Table 1 also shows the crystallite size of anatase and rutile grains in the coatings. When the duration is prolonged, the sizes of both anatase and rutile grains in the MAO and UMAO coatings gradually increase. The longer duration and higher voltage (Figure 1) generate more heat on the surface. It was reported that more heat on the surface can facilitate the growth of grains.[47] During the microarc oxidation process, the solution can be stirred by ultrasonic, which accelerates the cooling of the electrolyte. Meanwhile, the shock wave, which is generated by the collapse of cavitation bubbles, effectively breaks the primary crystallites and produces an extra artificial crystal nucleus.[40] Furthermore, the ultrasonic can increase the degree of undercooling of the melt, resulting in easier nucleation. This is similar to other metals during solidification.[2,40,48] Therefore, UMAO coatings have finer grains than MAO coatings.

2.4. Microhardness Tests

Figure 7 shows the microhardness of samples. The substrate has the minimum hardness (366 ± 8 HV). The MAO and UMAO samples have higher microhardness than the substrate due to the formation of oxide coatings. The thicknesses of coatings increase with extending the duration (Figure 3), increasing the hardness of both samples. MAO-5, MAO-10, and MAO-15, respectively, have the hardness of 396 ± 40, 435 ± 52, and 586 ± 84 HV. In comparison, UMAO-5, UMAO-10, and UMAO-15 have the hardness of 453 ± 28, 538 ± 35, and 706 ± 41 HV. UMAO coatings have finer grains than their MAO counterparts (Table 1), leading to the refinement strengthening.[49–51] Therefore, combining the results of larger thickness and finer grains, it is reasonable to understand that UMAO coatings have higher hardness compared with their MAO counterparts. Likewise, the MAO coating is a porous and uneven ceramic layer, while the ultrasonic can smoothen the surface of the coatings (Figure 2). Therefore, the MAO coatings show relatively larger deviation in hardness.

2.5. Electrochemical Measurements

The potentiodynamic polarization curves of MAO and UMAO samples in Hank's solution at $37\,°C$ are shown in **Figure 8** and the fitting results of corrosion current density (I_{corr}) and corrosion potential (E_{corr}) are shown in **Table 2**. The substrate has the lowest E_{corr} and the largest I_{corr} among all samples, which means that the substrate is prone to be corroded and has the highest corrosion rate.[52] Microarc oxidation can generate a coating composed of corrosion-resistant products (such as TiO_2). The generated coating protects the substrate from the ingressive ions in the environment. Therefore, the I_{corr} values of both MAO and UMAO samples decrease and the E_{corr} values increase with the extension of duration. In addition, the UMAO samples have higher E_{corr} and lower I_{corr} than the MAO counterparts. As mentioned earlier, the UMAO coatings have smaller pores and fewer cracks, which can hinder the ion exchange between the environment and the substrate.[43] Meanwhile, UMAO coatings have larger thicknesses (Figure 3), which extend the diffusion paths for the ingressive ions.[53,54] Therefore, ultrasonic can enhance the corrosion resistance of coatings by increasing their thicknesses and reducing the flaws in their microstructures.

The impedance characteristics of the coatings were examined by electrochemical impedance spectroscopy (EIS) (**Figure 9**). As seen from the Nyquist plot (Figure 9a,b), the samples have two capacitive loops. Meanwhile, the bode phase plots show two peaks (Figure 9d). These findings indicate a two-layer structure of both MAO and UMAO coatings: one is the outer porous layer and the other is the inner compact layer.[15,55] Therefore, an equivalent circuit model with two constant phase elements is applied to fit the data of EIS results (Figure 9a, inset).[56] Herein, R_s is the solution resistance. The constant phase elements of CPE_1 and CPE_2 simulate the electrical properties of the outer and inner layers, respectively. R_1 and R_2, which are paralleled with CPE_1 and CPE_2, represent the resistance of the outer layer and inner barrier layer.

The fitted data of EIS are shown in **Table 3**. As shown in Table 3, R1 increases when the duration is augmented.
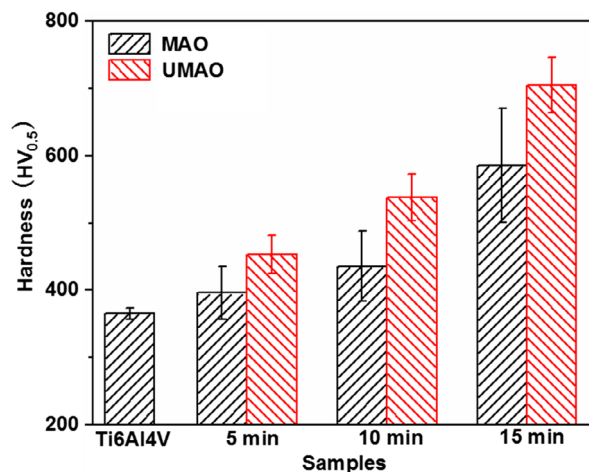

Figure 7. Microhardness of the coating samples and the substrate. MAO indicates the microarc oxidized samples without ultrasonic assistance; UMAO means the microarc oxidized samples with ultrasonic assistance.
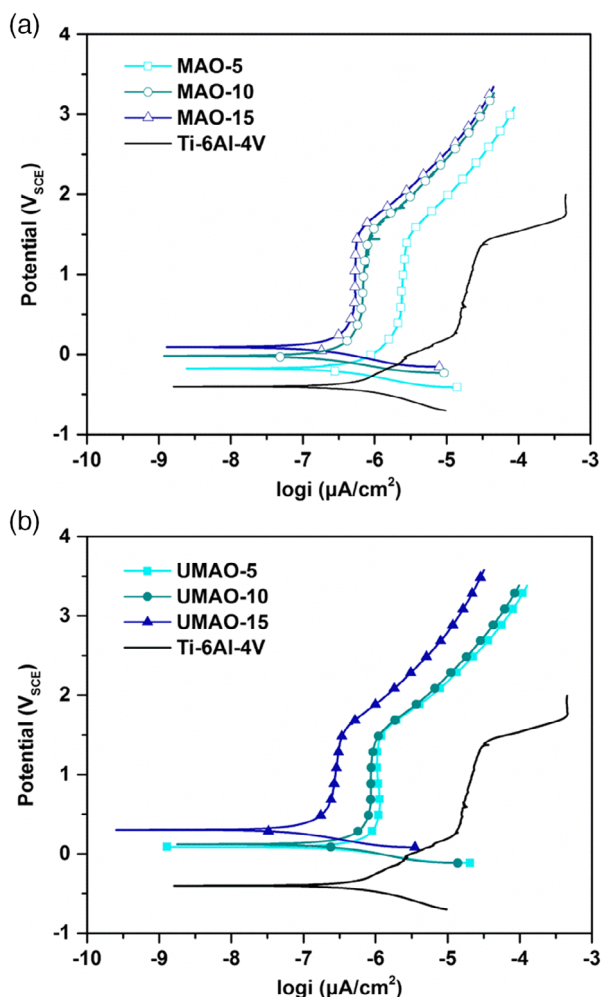
Figure 8. Potentiodynamic polarization curves of a) MAO and b) UMAO samples in Hank's solution at 37 °C. MAO-5, MAO-10, and MAO-15 indicate the microarc oxidized samples without ultrasonic assistance under the duration of 5, 10, and 15 min; UMAO-5, UMAO-10, and UMAO-15 mean the microarc oxidized samples with ultrasonic assistance under the duration of 5, 10, and 15 min.

Table 2. Fitted corrosion potentials (E_{corr}) and corrosion current densities (I_{corr}) of all samples in Hank's solution at 37 °C. MAO-5, MAO-10, and MAO-15 indicate the microarc oxidized samples without ultrasonic assistance under the duration of 5, 10, and 15 min; UMAO-5, UMAO-10, and UMAO-15 mean the microarc oxidized samples with ultrasonic assistance under the duration of 5, 10, and 15 min.

Samples	E_{corr} [V_{SCE}]	I_{corr} [$\mu A\ cm^{-2}$]
Ti–6Al–4V	-0.394 ± 0.019	0.493 ± 0.029
MAO-5	-0.176 ± 0.011	0.295 ± 0.031
MAO-10	-0.019 ± 0.008	0.236 ± 0.020
MAO-15	0.091 ± 0.026	0.238 ± 0.054
UMAO-5	0.089 ± 0.012	0.283 ± 0.032
UMAO-10	0.122 ± 0.015	0.145 ± 0.018
UMAO-15	0.309 ± 0.081	0.103 ± 0.014

Because of the two-layer structure of the microarc oxidation coating, the outer porous layer was easily permeated by the solution. According to the definition of electric resistance, R_1 is in direct proportion to the thickness of the coating and is inversely proportional to the pore size.[55] Therefore, in terms of Figure 5, the pore sizes increase with increasing the duration. Therefore, R_1 is supposed to decrease. According to the cross-sectional morphologies of the coatings (Figure 2), the thickness increases with an increase in the duration. Therefore, R_1 increases with increasing coating thickness. Meanwhile, the UMAO samples have larger thicknesses and smaller pores (Figure 2, 4, and 5) than the MAO counterparts. Therefore, the UMAO-5, UMAO-10, and UMAO-15 have larger R_1 values than the MAO-5, MAO-10, and MAO-15.

The total resistance of the coating is the sum of R_1 and R_2.[55,57] As shown in Table 3, R2 is significantly larger than R_1. Therefore, the corrosion resistance of microarc oxidation coating largely relies on the inner layer. The R_2 values of the samples also increase with the extension of duration (Table 3). Compared with the MAO samples, the cross-sectional morphologies of UMAO samples reveal smaller pores and fewer cracks (Figure 2). As such, UMAO samples have higher R_2 values than MAO counterparts, indicating that the UMAO samples have better corrosion resistance than MAO samples. This conclusion follows the results of the potentiodynamic polarization test and morphology analysis.

2.6. Wear Performance

For Ti orthopedic implants, they are frequently worn by the adjacent muscle. Therefore, wear resistance is also a critical consideration for surface modified Ti and Ti alloys.[58–60] **Figure 10** shows the mass losses and friction coefficients of MAO, UMAO samples, and the Ti–6Al–4V substrate measured by tribological tests. The Ti–6Al–4V substrate has the largest mass loss in all samples, indicating the lowest wear resistance. The MAO samples show lower mass loss than the substrate due to the formation of the oxide coatings. In comparison, UMAO samples exhibit lower mass loss compared with the MAO counterparts. Such results specify that the UMAO samples have improved wear resistance and their wear resistance increases with increasing the duration. On the contrary, except for MAO-5, the friction coefficients of both MAO and UMAO samples have slight augment as compared with that of the substrate. Notably, the substrate used for tribological tests is polished, while the coated samples have rough surfaces with a considerable number of pores. Because the MAO-5 coating is too thin, the friction coefficient of MAO-5 is very close to that of the substrate. As increasing the duration, the surfaces of MAO and UMAO samples become rougher (Figure 4). Therefore, such rough surfaces increase the friction coefficients of MAO and UMAO samples. Apart from the MAO-5 and UMAO-5 samples, the UMAO samples have relatively lower friction coefficients than the MAO counterparts due to the lower surface roughness (Figure 4). The MAO-5 and UMAO-5 samples have comparable roughness. As shown in Figure 2, the UMAO-5 contains smaller cracks and pores than the MAO-5, illustrating that the UMAO-5 coating is more compact than the MAO-5 coating. Consequently, the loose coating on
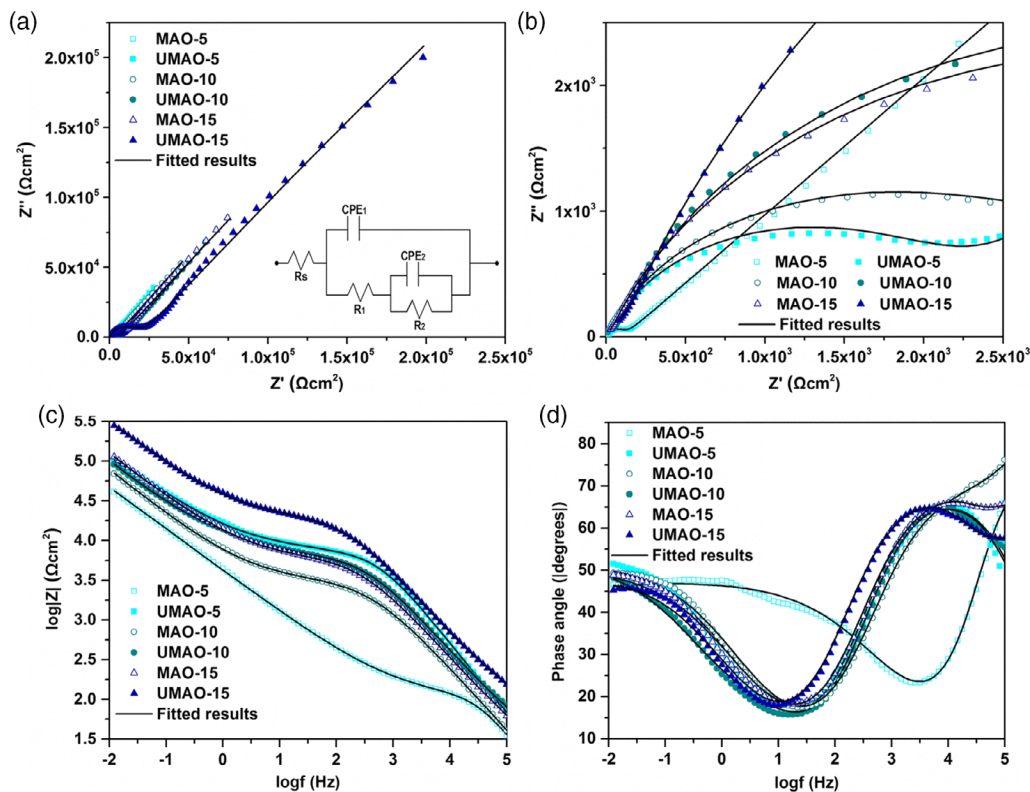
Figure 9. EIS of MAO and UMAO samples in Hank's solution at 37 °C: a) Nyquist plots, b) partial enlarged picture of (a), c) Bode impedance plots, and d) Bode angle plots. Inset: The equivalent circuit model. MAO-5, MAO-10, and MAO-15 indicate the microarc oxidized samples without ultrasonic assistance under the duration of 5, 10, and 15 min; UMAO-5, UMAO-10, and UMAO-15 mean the microarc oxidized samples with ultrasonic assistance under the duration of 5, 10, and 15 min.

Table 3. Fitted data of EIS results. CPE_1 and CPE_2: the constant phase elements; R_1: the outer layer resistance; R_2: the inner layer resistance; Y_0 is the corresponding CPE admittance.

Samples	CPE_1		R_1 [$k\Omega\ cm^2$]	CPE_2		R_2 [$k\Omega\ cm^2$]
	Y_0 [$\Omega^{-1}\ cm^{-2}s^n$]	n_1		Y_0 [$\Omega^{-1}\ cm^{-2}s^n$]	n_2	
MAO-5	$(7.62 \pm 0.12) \times 10^{-6}$	0.93 ± 0.03	0.13 ± 0.05	$(9.56 \pm 0.54) \times 10^{-5}$	0.54 ± 0.02	$(1.38 \pm 0.16) \times 10^{0}$
MAO-10	$(4.96 \pm 2.22) \times 10^{-7}$	0.80 ± 0.02	5.88 ± 0.81	$(4.34 \pm 0.41) \times 10^{-5}$	0.53 ± 0.03	$(1.72 \pm 0.77) \times 10^{1}$
MAO-15	$(4.43 \pm 0.99) \times 10^{-7}$	0.77 ± 0.01	6.03 ± 0.69	$(2.72 \pm 1.57) \times 10^{-5}$	0.56 ± 0.01	$(1.64 \pm 0.41) \times 10^{2}$
UMAO-5	$(2.10 \pm 0.42) \times 10^{-6}$	0.87 ± 0.04	2.46 ± 0.24	$(9.17 \pm 1.15) \times 10^{-5}$	0.57 ± 0.01	$(1.52 \pm 0.33) \times 10^{1}$
UMAO-10	$(6.95 \pm 0.55) \times 10^{-7}$	0.74 ± 0.05	6.68 ± 0.96	$(6.68 \pm 0.59) \times 10^{-5}$	0.56 ± 0.02	$(2.41 \pm 0.51) \times 10^{1}$
UMAO-15	$(2.65 \pm 0.45) \times 10^{-8}$	0.71 ± 0.04	19.50 ± 2.15	$(2.36 \pm 1.20) \times 10^{-5}$	0.57 ± 0.04	$(4.30 \pm 1.13) \times 10^{3}$

MAO-5 has a relatively lower hardness and cannot sustain the pressure of the friction pair. As such, UMAO-5 shows the lower mass loss compared with MAO-5. Similar results are also found for UMAO-10 and UMAO-15.

After the tribological tests, the wear tracks of each sample were observed by SEM, as shown in **Figure 11**. The light blue dashes indicate the widths of wear tracks on the samples. Figure 11a demonstrates that the Ti–6Al–4V substrate has the widest wear track among all samples, which means that the Ti–6Al–4V substrate is prone to be worn. Many parallel grooves are presented on the wear track, illustrating a typical abrasive wear feature.[61] As shown in Figure 2a and 4a, the MAO-5 coating has the

smallest thickness and many cracks and pores are presented in the coating. As a result, the MAO-5 coating does not have enough resistance to friction. As shown in Figure 11d, the MAO-10 coating shows narrower wear tracks. Grooves are also found on the wear tracks on the MAO-10. Such morphologies on the wear tracks of MAO-5 and MAO-10 are similar to that of the substrate, indicating that the coatings are completely worn out. However, the coating is still presented on the surface of MAO-15 (Figure 11f), specifying that the wear resistance of MAO coatings increases with increasing the duration. Figure 11c shows that the UMAO-5 is partially spalled. Although the remnant coating is full of cracks, it still adheres to the substrate. The UMAO-10 and
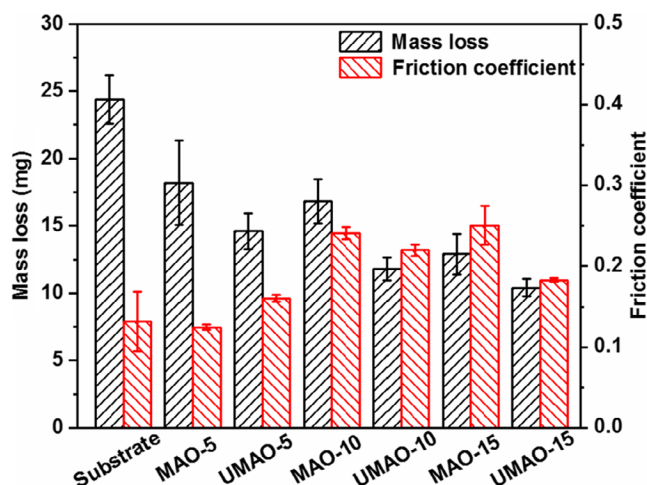
Figure 10. Mass loss and friction coefficient for different MAO samples and the substrate. MAO-5, MAO-10, and MAO-15 indicate the microarc oxidized samples without ultrasonic assistance under the duration of 5, 10, and 15 min; UMAO-5, UMAO-10, and UMAO-15 mean the microarc oxidized samples with ultrasonic assistance under the duration of 5, 10, and 15 min.

UMAO-15 samples present similar wear features with many cracks on the coating surface but almost no spalling (Figure 11e,g). This finding demonstrates that slight fatigue wear takes place on the UMAO-10 and UMAO-15 coatings.[62–64] Furthermore, the narrower wear tracks on the UMAO samples illustrate their better wear resistance, which is consistent with the results in Figure 10. The ultrasonic assistance in the microarc oxidation of Ti–6Al–4V results in thicker coatings with higher hardness and fewer cracks. The coatings with such features also improve their wear resistance.

2.7. Cell Proliferation

As stated earlier, the MAO-15 and UMAO-15 samples possess best corrosion and wear resistance in the corresponding groups. Due to this reason, the MAO-15 and UMAO-15 samples were selected for the cell proliferation experiments. The results are shown in **Figure 12**. Both MAO-15 and UMAO-15 show larger number of cells than the original planted cells. This means that the microarc oxidation coatings of Ti–6Al–4V produced in biological electrolyte offer a biologically favorable environment. It is known that the surface geometry (such as roughness, pore size, and so on) of implant has also a significant influence on the cell proliferation behavior.[25] Sanchez et al.[65] investigated the biological behavior of porous Ti scaffolds with different ranges of pore sizes and found that small pores benefit for cell attachment in the first 3 days. As shown in Figure 4 and 5, the UMAO-15 shows lower mean area of pores compared with the MAO-15. Meanwhile, for TiO_2 coatings produced by microarc oxidation, the increased surface roughness would lower the cell proliferation rate.[25] As shown in Figure 4, the UMAO-15 surface has a lower roughness. Therefore, the proliferation rate of cell on the UMAO-15 sample is higher than that on the MAO-15 (Figure 12). Based on these two features, one can conclude that the ultrasonic

assistance has a positive influence on the microarc oxidation coatings on Ti–6Al–4V.

3. Conclusions

In this work, the wear- and corrosion-resistant coatings on Ti–6Al–4V alloy for potential biomedical applications were, respectively, synthesized by microarc oxidation with and without ultrasonic assistance in Hank's solution. Different durations of 5, 10, and 15 min were used. The microstructures, hardness, corrosion resistance, and wear performance of the produced coatings were systematically examined. Some key conclusions can be drawn as follows: 1) Ultrasonic assistance decreases the breakdown voltage of the formed oxide coating on the Ti–6Al–4V substrate. The breakdown voltage of traditional microoxidation coatings and ultrasonic-assisted microarc oxidation coatings are 250 and 213 V, respectively. 2) Ultrasonic can stir the electrolyte and accelerate its cooling rate during the microarc oxidation process. The molten metal can be solidified before the formation of the subsequent ceramic layer and the production of internal flaws in the coatings is therefore reduced. Consequently, the ultrasonic-assisted coatings have homogeneous microstructures. 3) Ultrasonic assistance promotes the growth of the coatings. Due to the cavitation effect of ultrasonic, the number of pores on the coating surfaces increases while the pore size decreases. It is also speculated that ultrasonic can break up the formed nucleus to increase the number of crystal nuclei. Therefore, the ultrasonic-assisted coatings have finer grains. 4) Due to their higher thickness and fewer flaws, the ultrasonic-assisted coatings show better corrosion resistance in the Hank's solution. The ultrasonic-assisted microarc oxidation coatings reveal higher corrosion potential, lower corrosion current density, and higher impedance compared with the coatings without ultrasonic assistance. 5) Due to the finer grains, the ultrasonic-assisted coatings exhibit higher hardness and better wear resistance. After the 900 s tribology test at room temperature, the conventional microarc oxidation coatings with 5 and 10 min durations are worn out. In comparison, the ultrasonic-assisted coatings with 5 min duration still adhere to the substrate. The ultrasonic-assisted one with 15 min duration shows a lower mass loss (by 25.1%) compared with the counterpart. 6) The microarc oxidation coatings produced with ultrasonic assistance show better cell proliferation in the first 4 days compared with the conventional microarc oxidation coating, which contributes to their lower mean area of pores and lower surface roughness.

4. Experimental Section

Preparation of Samples: An annealed Ti–6Al–4V alloy (6.19 wt% Al, 4.10 wt% V, 0.04 wt% Fe, 0.01 wt% H, 0.01 wt% C, 0.05 wt% O, and Ti balanced) sheet was used as the substrate. Samples with the dimensions of 15 mm × 15 mm × 5 mm were machined for the microarc oxidation process. A 3 mm-diameter tapped hole was drilled on one side of each sample. Before the microarc oxidation process, the samples were ground by alumina abrasive paper up to 1500 grits and cleaned in an ultrasonic bath with acetone and ethyl alcohol at room temperature for 10 min. At last, a 3 mm-diameter cylindrical copper wire, which was covered by insulation paint, was inserted into the sample in the drilled hole. The biological electrolyte system was prepared by distilled water, which contains 6 g L^{-1}
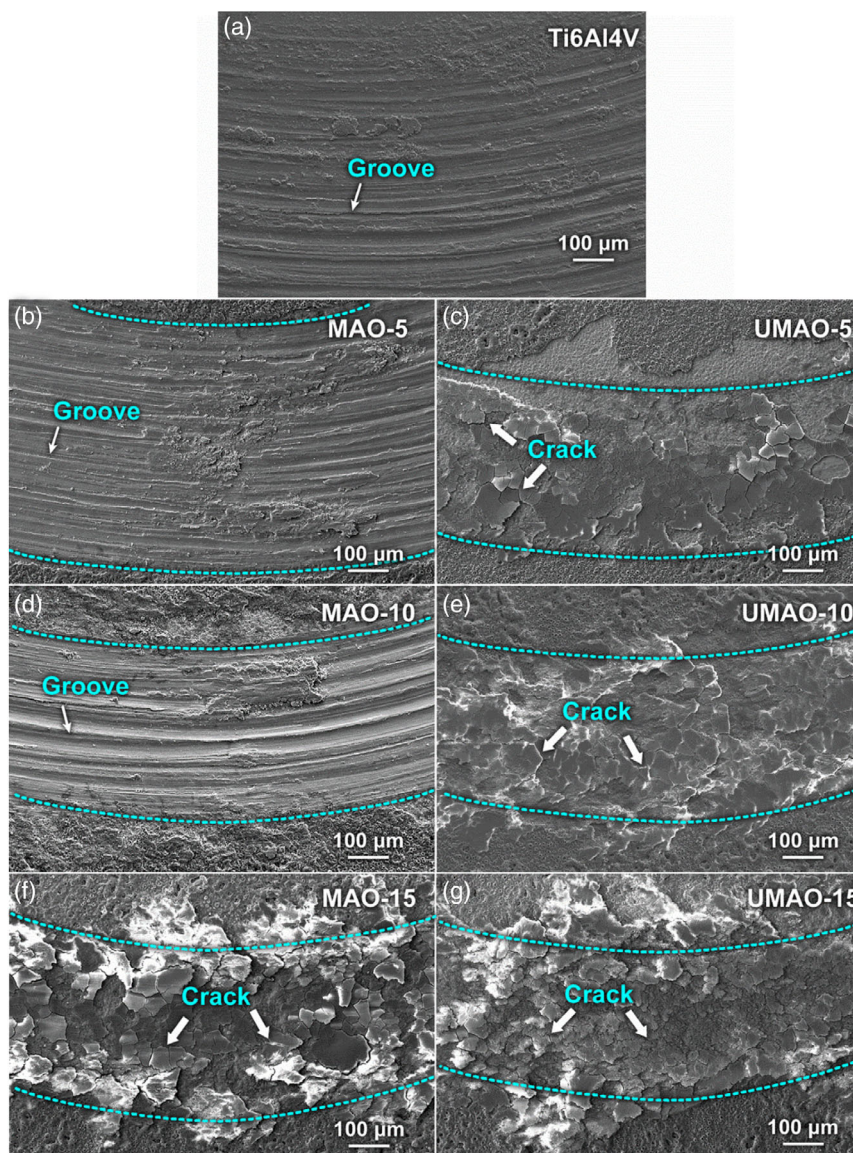
Figure 11. SEM images of the wear tracks of samples: a) Ti–6Al–4V substrate, b) MAO-5, c) UMAO-5, d) MAO-10, e) UMAO-10, f) MAO-15, and g) UMAO-15. The light blue dashes indicate the widths of wear tracks on the samples. MAO-5, MAO-10, and MAO-15 indicate the microarc oxidized samples without ultrasonic assistance under the duration of 5, 10, and 15 min; UMAO-5, UMAO-10, and UMAO-15 mean the microarc oxidized samples with ultrasonic assistance under the duration of 5, 10, and 15 min.

Na_2SiO_3, 1 g L^{-1} $C_2H_5CaO_3$, 0.8 g L^{-1} $(NaPO_3)_6$, and 0.55 g L^{-1} NaH_2PO_4 at 40–50 °C. The Ca and P contained in biological electrolytes would be incorporated in the produced oxide coatings. It is known that the sample surface with appropriate Ca/P ratio optimizes the osteoblast viability and promotes the alkaline phosphatase activity in osteoblasts.[66] For comparison, the microarc oxidation samples, respectively, were produced with and without ultrasonic assistance.

Microarc Oxidation: WHD-20 MAO system was used in this work. Ti–6Al–4V sample was used as the anode, and the stainless steel sheet was worked as the cathode. To achieve enough thickness of coatings, the constant current mode was used in this work. The microarc oxidation processes were conducted with the current density of 60 mA cm^{-2}, frequency of 600 Hz, duty cycle of 40%, and microarc oxidation durations of 5, 10, and 15 min, respectively. MAO indicates the microarc oxidized samples without ultrasonic assistance; UMAO means the microarc oxidized samples with ultrasonic assistance. In the following, the simply microarc oxidized (MAOed) samples with the microarc oxidation duration of 5, 10, and 15 min are denoted as MAO-5, MAO-10, and MAO-15, respectively. Meanwhile, UMAO-5, UMAO-10, and UMAO-15, respectively, represent the MAOed samples with the ultrasonic assistance after the different microarc oxidation durations of 5, 10, and 15 min. To avoid wordiness, duration is used to stand for microarc oxidation duration in the following. Furthermore, a PS-40A ultrasonic cleaner was used as the source of ultrasonic during the microarc oxidation process. A beaker, which contained biological electrolyte and was used as a reaction vessel, was put in the sink of the ultrasonic cleaner. The water in the sink acted as the cooling medium to cool the biological electrolyte. The parameters of ultrasonic cleaner used in this work were as follows: power of 120 W and frequency of 40 kHz.
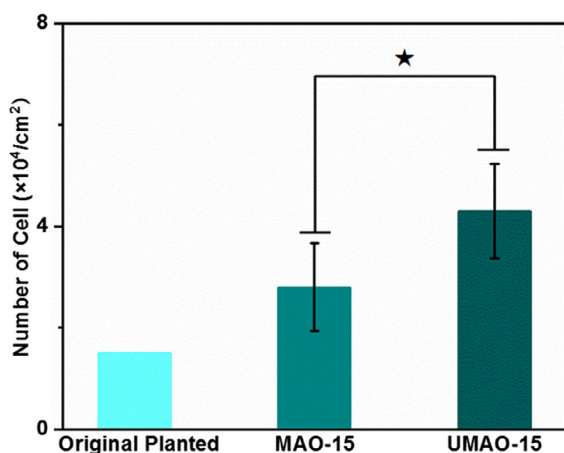
**ADVANCED
SCIENCE NEWS**

www.advancedsciencenews.com

**ADVANCED
ENGINEERING
MATERIALS**

www.aem-journal.com

Figure 12. MG-63 cell proliferation on different samples after cultivation for 4 days. ★ denotes significant differences ($p < 0.05$) between UMAO-15 group and MAO-15 group.

Characterizations: The microstructures of coatings were investigated using a JSM-6480 SEM) equipped with EDS. The samples for cross-sectional observations were sealed with epoxy resin. Afterward, the cross section of samples was ground and polished in terms of standard metallographic technique. The samples for surface observations were merely cleaned by distilled water and dried after the microarc oxidation process. Before conducting the SEM observations, the samples were sputtered a gold layer due to the insulation of ceramic coating. The mean areas of pores were measured by the software Image J. Meanwhile, the porosity, which is the percentage of total pore area to the total surface area of the sample, was also measured by Image J. The roughness of the coating was measured by laser confocal. The phase constituents of samples were analyzed by a DX-2700 XRD instrument with a monochromatic Cu Kα source. XRD parameters were set as follows: scanning range of 20°–80°, scanning speed of 4° min^{-1}, and a step size of 0.02°. The XRD data were analyzed by the software Jade 6.5. The diffraction profiles were corrected for the instrumental broadening using a corundum sample. Meanwhile, to analyze the influence of ultrasonic assistance on the volume fraction of each phase in the coatings, the following formula was used:[67–69]

$$V_{f,i} = A_i \left(\sum A_i \right)^{-1} \qquad (1)$$

where $V_{f,i}$ is the volume fraction of the phase, A_i is the total area of the phase, and ΣA_i is the total area of all phases in an XRD pattern. To calculate the size of oxide grains in the coatings, the Scherrer formula was used:[70]

$$D_{hkl} = K\lambda (B_{hkl}\cos\theta)^{-1} \qquad (2)$$

where D_{hkl} represents crystallite size in the direction perpendicular to (hkl) plane, K is a numerical value (0.9 used in this work[70]), λ is the wavelength of X-ray (Cu-target, $\lambda = 1.54$ nm), B_{hkl} is the full width at half maximum of XRD peak (in radian), and θ is the Bragg angle. According to the XRD pattern detected, the (101) plane of anatase and (110) plane of rutile were used to calculate their crystallite size.

Electrochemical Measurements: The corrosion resistance of MAOed samples and Ti–6Al–4V substrate were examined using a three-electrode electrochemical workstation (CHI660E, Chenhua Co. Ltd., Shanghai). The sample with an area of 1 cm^2 in the middle of the surface was used as the working electrode, and the other region was sealed with insulating paste. An open circuit potential (OCP) test was conducted for 1800 s to ensure the stability of the samples in the electrolyte. Subsequently, the EIS measurement using an alternating signal of 10 mV from 10^{-2} to 10^5 Hz was

performed. The EIS data were fitted by Zview software. The potentiodynamic polarization tests were conducted using the following parameters: scanning rate of 1 mV s^{-1} and potential range of −0.5 to +3 V (vs OCP). The potentiodynamic polarization curves were fitted by Zsimpwin software. Hank's solution, which is a classical type of simulated body fluid, was used electrolyte in the electrochemical measurement. The pH of Hank's solution, which contained 8.00 g L^{-1} NaCl, 0.14 g L^{-1} CaCl$_2$, 0.40 g L^{-1} KCl, 0.35 g L^{-1} NaHCO$_3$, 1.00 g L^{-1} glucose, 0.1 g L^{-1} MgCl$_2$·6H$_2$O, 0.06 g L^{-1} Na$_2$HPO$_4$·2H$_2$O, 0.06 g L^{-1} KH$_2$PO$_4$, and 0.06 g L^{-1} MgSO$_4$·7H$_2$O, was adjusted to 7.35 by the diluted HCl and NaOH. All electrochemical tests were operated at 37 ± 0.5 °C. The electrochemical tests were repeated at least 3 times for data reproducibility.

Tribological Test: The wear resistance of MAOed coatings and Ti–6Al–4V substrate were measured by pin-on-disc tribological test at room temperature without lubrication in air. The testing parameters were as follows: 3 mm friction radius, 10 N load, Si$_3$N$_4$ ball in 10 mm diameter, 100 rpm sliding speed, and 900 s testing time. Measurements were conducted 3 times to ensure reproducibility. The wear loss of each sample was measured by a balance with an accuracy of 0.01 mg. The wear tracks were observed by SEM.

Cell Proliferation: The samples using 15 min duration were selected for cell proliferation test. The human osteoblast-like cells (MG-63, iCell Bioscience Inc., China) were cultured on the samples to investigate the cell proliferation. Before conducting the cell proliferation experiment, the samples were put into a 30 mm petri dish and one side of the samples was irradiated by UV light for 0.5 h. Subsequently, another side of the samples was also irradiated for 0.5 h. The presuscitated cell lined implant onto the samples with the destiny of 1.5×10^4 cells cm^{-2}. The cultured samples were incubated in a 5% CO$_2$ humidified box at 37 °C, supplementing with 10% fetal bovine serum as a culturing medium.

The proliferation behavior was evaluated by counting the number of cells after cultivating cells for 4 days. The cells were separated from the samples with 0.05% trypsin-ethylenediaminetetraacetic acid (trypsin-EDTA) solution and counted with a hemocytometer. The cell layers were washed by Hank's balanced salt solution and segregated with a trypsin-EDTA solution. After centrifugation at 1200 rpm for 7 min, the cell pellets were washed once again by Hank's balanced salt solution and resuspended by overtaxing them in 0.1% Triton X-100. The pellets were split through 4 cycles of continuous freezing and thawing.

Conflict of Interest

The authors declare no conflict of interest.

Author Contribution

C.X.: Conceptualization, investigation, visualization, writing original draft, and writing—review and editing; **L.-Y.C.:** conceptualization, project administration, supervision, and writing—review and editing; **C.-B.Z.:** conceptualization and supervision; **H.-Y.Z.:** investigation; **C.-H.Z.:** data curation; **Z.-X.W.:** investigation and data curation; **S.L.:** writing—review and editing; **J.-W.Z.:** investigation; **L.-C.Z.:** supervision and writing—review and editing.

Data Availability Statement

The raw/processed data required to reproduce these findings cannot be shared at this time as the data also form part of an ongoing study.

Keywords

[1] L. C. Zhang, L. Y. Chen, *Adv. Eng. Mater.* **2019**, *21*, 1801215.

[2] L. C. Zhang, J. Xu, E. Ma, *Mater. Sci. Eng., A* **2006**, *434*, 280.

[3] C. D. Rabadia, Y. J. Liu, C. H. Zhao, J. C. Wang, S. F. Jawed, L. Q. Wang, L. Y. Chen, H. Sun, L. C. Zhang, *Mater. Sci. Eng., A* **2019**, *766*, 138340.

[4] L. C. Zhang, J. Xu, *J. Non Cryst. Solids* **2004**, *347*, 166.

[5] C. D. Rabadia, Y. J. Liu, L. Y. Chen, S. F. Jawed, L. Q. Wang, H. Sun, L. C. Zhang, *Mater. Des.* **2019**, *179*, 107891.

[6] S. Liu, J. Liu, L. Wang, R. L.-W. Ma, Y. Zhong, W. Lu, L.-C. Zhang, *Scr. Mater.* **2020**, *181*, 121.

[7] L. M. Kang, C. Yang, *Adv. Eng. Mater.* **2019**, *21*, 1801359.

[8] X. Luo, L. H. Liu, C. Yang, H. Z. Lu, H. W. Ma, Z. Wang, D. D. Li, L. C. Zhang, Y. Y. Li, *J. Mater. Sci. Technol.* **2021**, *68*, 112.

[9] S. Zhao, S. J. Li, S. G. Wang, W. T. Hou, Y. Li, L. C. Zhang, Y. L. Hao, R. Yang, R. D. K. Misra, L. E. Murr, *Acta Mater.* **2018**, *150*, 1.

[10] N. Dai, J. Zhang, Y. Chen, L.-C. Zhang, *J. Electrochem. Soc.* **2017**, *164*, C428.

[11] M.-T. Tsai, Y.-W. Chen, C.-Y. Chao, J. S. C. Jang, C.-C. Tsai, Y.-L. Su, C.-N. Kuo, *J. Alloys Compd.* **2020**, *816*, 152615.

[12] Y. Liu, P. Jin, J. Li, T. Lin, F. Li, S. Hou, Q. Sun, J. Feng, *Adv. Eng. Mater.* **2020**, *22*, 2000187.

[13] L. M. Kang, Y. J. Cai, X. C. Luo, Z. J. Li, X. B. Liu, Z. Wang, Y. Y. Li, C. Yang, *Scr. Mater.* **2021**, *193*, 43.

[14] L. C. Zhang, Y. Liu, S. Li, Y. Hao, *Adv. Eng. Mater.* **2018**, *20*, 1700842.

[15] Y. Bai, X. Gai, S. Li, L. C. Zhang, Y. Liu, Y. Hao, X. Zhang, R. Yang, Y. Gao, *Corros. Sci.* **2017**, *123*, 289.

[16] P. Yadav, T. Bock, Z. Fu, H. Lorenz, I. Gotman, P. Greil, N. Travitzky, *Adv. Eng. Mater.* **2020**, *22*, 2000408.

[17] L.-C. Zhang, L.-Y. Chen, L. Wang, *Adv. Eng. Mater.* **2020**, *22*, 1901258.

[18] I. Izquierdo-Barba, L. Santos-Ruiz, J. Becerra, M. J. Feito, D. Fernández-Villa, M. C. Serrano, I. Díaz-Güemes, B. Fernández-Tomé, S. Enciso, F. M. Sánchez-Margallo, D. Monopoli, H. Afonso, M. T. Portolés, D. Arcos, M. Vallet-Regí, *Acta Biomater.* **2019**, *83*, 456.

[19] B. Wu, Z. Pan, S. Li, D. Cuiuri, D. Ding, H. Li, *Corros. Sci.* **2018**, *137*, 176.

[20] X. Zhang, Z. Yao, Z. Jiang, Y. Zhang, X. Liu, *Corros. Sci.* **2011**, *53*, 2253.

[21] P. Heinl, L. Müller, C. Körner, R. F. Singer, F. A. Müller, *Acta Biomater.* **2008**, *4*, 1536.

[22] D. B. Wei, P. Z. Zhang, Z. J. Yao, W. P. Liang, Q. Miao, Z. Xu, *Corros. Sci.* **2013**, *66*, 43.

[23] E. H. Valente, M. S. Jellesen, M. A. J. Somers, T. L. Christiansen, *Surf. Coat. Technol.* **2020**, *383*, 125278.

[24] L.-C. Zhang, Z. Jia, F. Lyu, S.-X. Liang, J. Lu, *Prog. Mater. Sci.* **2019**, *105*, 100576.

[25] L. H. Li, Y. M. Kong, H. W. Kim, Y. W. Kim, H. E. Kim, S. J. Heo, J. Y. Koak, *Biomaterials* **2004**, *25*, 2867.

[26] X. Ly, S. Yang, T. Nguyen, *Surf. Coat. Technol.* **2020**, *395*, 125923.

[27] Z. X. Wang, G. Q. Chen, L. Y. Chen, L. Xu, S. Lu, *Metals* **2018**, *8*, 724.

[28] C. Y. Li, X. L. Feng, X. L. Fan, X. T. Yu, Z. Z. Yin, M. B. Kannan, X. B. Chen, S. K. Guan, J. Zhang, R. C. Zeng, *Adv. Eng. Mater.* **2019**, *21*, 1900446.

[29] X. Liu, P. K. Chu, C. Ding, *Mater. Sci. Eng., R* **2004**, *47*, 49.

[30] Z. Yao, F. Jia, S. Tian, C. Li, Z. Jiang, X. Bai, *ACS Appl. Mater. Interfaces* **2010**, *2*, 2617.

[31] H. F. Guo, M. Z. An, H. B. Huo, S. Xu, L. J. Wu, *Appl. Surf. Sci.* **2006**, *252*, 7911.

[32] O. Hyeong Kwon, A. Kikuchi, M. Yamato, T. Okano, *Biomaterials* **2003**, *24*, 1223.

[33] L. Benea, A. Răvoiu, J.-P. Celis, *ACS Biomater. Sci. Eng.* **2019**, *5*, 5925.

[34] L. Qu, M. Li, M. Liu, E. Zhang, C. Ma, *J. Adv. Ceram.* **2013**, *2*, 227.

[35] H. F. Guo, M. Z. An, *Appl. Surf. Sci.* **2005**, *246*, 229.

[36] Y. M. Wang, L. X. Guo, J. H. Ouyang, Y. Zhou, D. C. Jia, *Appl. Surf. Sci.* **2009**, *255*, 6875.

[37] S. Lu, L. Tang, X. Z. Jiang, Z. X. Wang, J. Chen, *Adv. Mater. Res.* **2011**, *337*, 101.

[38] G. Cao, H. Konishi, X. Li, *Mater. Sci. Eng., A* **2008**, *486*, 357.

[39] M. A. Vasylyev, S. P. Chenakin, L. F. Yatsenko, *Acta Mater.* **2012**, *60*, 6223.

[40] V. Abramov, O. Abramov, V. Bulgakov, F. Sommer, *Mater. Lett.* **1998**, *37*, 27.

[41] S. Dejiu, C. Jingrui, L. Guolong, H. Donglei, W. Lailei, M. Haojie, X. Yonghong, C. He, C. Yaqian, *Vacuum* **2014**, *99*, 143.

[42] D. Shen, D. He, F. Liu, C. Guo, J. Cai, G. Li, H. Ma, *Ultrasonics* **2014**, *54*, 1065.

[43] R. Xie, N. Lin, P. Zhou, J. Zou, P. Han, Z. Wang, B. Tang, *Appl. Surf. Sci.* **2018**, *436*, 467.

[44] L. Zhao, C. Cui, Q. Wang, S. Bu, *Corros. Sci.* **2010**, *52*, 2228.

[45] R. F. Zhang, S. F. Zhang, *Corros. Sci.* **2009**, *51*, 2820.

[46] Y. Xu, M. Y. Tan, *Corros. Sci.* **2019**, *151*, 163.

[47] L. Y. Chen, P. Sang, L. Zhang, D. Song, Y. Q. Chu, L. Chai, L. C. Zhang, *Metals* **2018**, *8*, 759.

[48] L. C. Zhang, J. Xu, J. Eckert, *J. Appl. Phys.* **2006**, *100*, 033514.

[49] L. Chen, J. Li, Y. Zhang, W. Lu, L. C. Zhang, L. Wang, D. Zhang, *J. Nucl. Sci. Technol.* **2016**, *53*, 496.

[50] M. Zhang, Y. N. Li, F. C. Zhang, X. B. Wang, L. Y. Chen, Z. N. Yang, *Mater. Sci. Eng. A* **2017**, *706*, 236.

[51] L. J. Chai, S. Y. Wang, H. Wu, N. Guo, H. C. Pan, L. Y. Chen, K. L. Murty, B. Song, *Sci. China Technol. Sci.* **2017**, *60*, 1255.

[52] J. Lei, C. Shi, S. Zhou, Z. Gu, L.-C. Zhang, *Surf. Coat. Technol.* **2018**, *334*, 274.

[53] L. Zhang, L. Y. Chen, C. Zhao, Y. Liu, L. C. Zhang, *Metals* **2019**, *9*, 850.

[54] L. Chen, J. Li, Y. Zhang, L.-C. Zhang, W. Lu, L. Zhang, L. Wang, D. Zhang, *Corros. Sci.* **2015**, *100*, 651.

[55] L. Chang, L. Tian, W. Liu, X. Duan, *Corros. Sci.* **2013**, *72*, 118.

[56] D. He, G. Li, D. Shen, C. Guo, H. Ma, J. Cai, *Vacuum* **2014**, *107*, 99.

[57] P. Qin, Y. Chen, Y.-J. Liu, J. Zhang, L.-Y. Chen, Y. Li, X. Zhang, C. Cao, H. Sun, L.-C. Zhang, *ACS Biomater. Sci. Eng.* **2019**, *5*, 1141.

[58] R. Yazdi, H. M. Ghasemi, C. Wang, A. Neville, *Corros. Sci.* **2017**, *128*, 23.

[59] K. Xiang, L.-Y. Chen, L. Chai, N. Guo, H. Wang, *Appl. Surf. Sci.* **2020**, *517*, 146214.

[60] L. Y. Chen, Y. W. Cui, L. C. Zhang, *Metals* **2020**, *10*, 1139.

[61] L.-Y. Chen, H. Wang, C. Zhao, S. Lu, Z.-X. Wang, J. Sha, S. Chen, L.-C. Zhang, *Surf. Coat. Technol.* **2019**, *369*, 31.

[62] Q. Wang, C. Ramírez, C. S. Watts, O. Borrero-López, A. L. Ortiz, B. W. Sheldon, N. P. Padture, *Acta Mater.* **2020**, *186*, 29.

[63] S.-X. Liang, X. Wang, W. Zhang, Y.-J. Liu, W. Wang, L.-C. Zhang, *Appl. Mater. Today* **2020**, *19*, 100543.

[64] J. Miao, L. C. Zhang, H. Lin, *Chem. Eng. Sci.* **2013**, *87*, 152.

[65] C. Torres-Sanchez, F. R. A. Al Mushref, M. Norrito, K. Yendall, Y. Liu, P. P. Conway, *Mater. Sci. Eng. C* **2017**, *77*, 219.

[66] H. Liu, H. Yazici, C. Ergun, T. J. Webster, H. Bermek, *Acta Biomater.* **2008**, *4*, 1472.

[67] C. D. Rabadia, Y. J. Liu, S. F. Jawed, L. Wang, Y. H. Li, X. H. Zhang, T. B. Sercombe, H. Sun, L. C. Zhang, *Mater. Des.* **2018**, *160*, 1059.

[68] L. Y. Chen, T. Xu, S. Lu, Z. X. Wang, S. Chen, L. C. Zhang, *Surf. Coat. Technol.* **2018**, *350*, 436.

[69] P. Sang, L. Y. Chen, C. Zhao, Z. X. Wang, H. Wang, S. Lu, D. Song, J. H. Xu, L. C. Zhang, *Metals* **2019**, *9*, 1342.

[70] U. Holzwarth, N. Gibson, *Nat. Nanotechnol.* **2011**, *6*, 534.

2001433 (14 of 14)